MAGNETOHYDRODYNAMICS Vol. 0 (1964), No. 0, pp. 1–10

Metal pad roll instability in liquid metal batteries

N. Weber[1], *P. Beckstein*[1], *V. Galindo*[1], *W. Herreman*[2], *C. Nore*[2], *F. Stefani*[1] *T. Weier*[1]

[1] *Helmholtz-Zentrum Dresden - Rossendorf, Bautzner Landstr. 400, 01328 Dresden, Germany*

[2] *Laboratoire d'Informatique pour la Mécanique et les Sciences de l'Ingénieur, CNRS UPR 3251, bât. 508, 91405 Orsay CEDEX and Université Paris-Sud 11, France*

The increasing deployment of renewable energies requires three fundamental changes to the electric grid: more transmission lines, a flexibilisation of the demand and grid scale energy storage. Liquid metal batteries (LMBs) are considered these days as a promising means of stationary energy storage. Built as a stable density stratification of two liquid metals separated by a liquid salt, LMBs have three main advantages: a low price, a long life-time and extremely high current densities. In order to be cheap, LMBs have to be built large. However, battery currents in the order of kilo-amperes may lead to magnetohydrodynamic (MHD) instabilities, which – in the worst case – may short-circuit the thin electrolyte layer. The metal pad roll instability, as known from aluminium reduction cells, is considered as one of the most dangerous phenomena for LMBs. We develop a numerical model, combining fluid- and electrodynamics with the volume-of-fluid method, to simulate this instability in cylindrical LMBs. We explain the instability mechanism similar to that in aluminium reduction cells and give some first results, including growth rates and oscillation periods of the instability[1].

1. Motivation According to prognoses of the International Energy Agency, the worldwide energy demand will grow from the year 2011 to 2035 by two thirds. In the same period, the share of renewable energies is predicted to rise from 20 to 31 % [2]. These renewable energies are highly fluctuating; in order to stabilise voltage and frequency in the electric grid, new transmission lines must be built

[1]This article is an extended version of a conference paper of the proceedings of the 10th PAMIR conference [1].

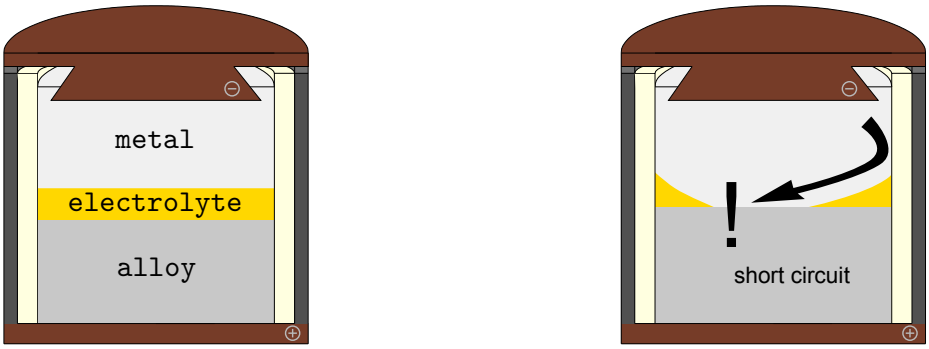

(a) (b)

Figure 1: Scheme of a liquid metal battery with typical inventory (a), and short circuit due to a strong fluid flow in the upper metal compartment (b).

and the demand should be flexibilised as much as possible. Furthermore, stationary energy storage on a large scale will become mandatory. Typical requirements for such storage devices are a low price (< 0.1€/kWh), a long life-time (> 7000 cycles), fast response times, and safety [3, 4, 5, 6]. Liquid metal batteries (LMBs) promise to fulfil these requirements [6]; they are high temperature batteries as e.g. sodium sulphur and ZEBRA ($NaNiCl_2$) cells [7, 8]. LMBs consist of a stable density stratification of two liquid metals, separated by a molten salt layer (Fig. 1a) [9, 10]. During discharge, the upper metal will donate electrons. The ion will cross the electrolyte layer and alloy with the bottom metal. If no corrosion occurs, the reaction should be fully reversible.

First liquid metal cells were operated in the 1960 by General Motors Corporation, Atomics International and Argonne National Laboratory mostly for the conversion of thermal to electric energy. Cairns [11] gives a short overview about these works; Crouthamel [10], Cairns [9], Swinkels [12] and Chum [13, 14] provide very detailed information. After some calm decades, liquid metal batteries were revived by the group of Donald Sadoway [5, 6] as grid scale energy storage devices. Their main argument for the deployment of LMBs is the low price of these cells.

As the active materials of LMBs are predicted to represent only 25 % of the cell cost, LMBs have to be built large, in order to be cheap. However, strong currents may lead to different instabilities. In the worst case, a strong fluid flow may wipe away the electrolyte layer and short-circuit the battery (Fig. 1b). Depending on the geometry of the current collectors, electro-vortex flow can be dangerous for batteries of a diameter larger than several decimetres [15]. The current-driven Tayler instability may appear, too, and lead to a short circuit in very large cells (diameter > 1 m and aspect ratio of the same order) [16, 17]. Further, the high resistance of the salt layer will lead to internal heat generation and thermal convection in the upper metal as well as the electrolyte layer, although the resulting flow is not expected to endanger the operation of small and medium sized cells [18]. Thermal convection was studied in addition with the intention to increase mass transfer in the lower metal and improve the efficiency of the cell [19, 20]. Concentration polarisation and even the formation of solid intermetallic phases are indeed important issues because this is often observed experimentally [9, 21, 22, 23, 24, 25, 26].

Long wave interface instabilities, also known as metal pad rolling or sloshing, may lead to a short-circuit even in small cells [27]. These instabilities are already known from aluminium smelters, where they limit the maximum electrolysis current [28, 29, 30, 31]. Here, we use an integro-differential MHD model [32] as already used to simulate the Tayler instability and electro-vortex flow, enhanced by multiphase support, to simulate metal pad rolling in a three layer model of a liquid metal battery.

2. Numerical model The single-phase model developed to describe the magnetohydrodynamic flow in one electrode of a liquid metal battery [32] is enhanced by multiphase support. It is implemented in the open source CFD library OpenFOAM and based on the standard solver multiphaseInterFoam [33].

The fluid flow in a viscous, electrically conducting and incompressible fluid of several phases is described by the Navier-Stokes equation

$$\frac{\partial(\rho \boldsymbol{u})}{\partial t} + \nabla \cdot (\rho \boldsymbol{u}\boldsymbol{u}) = -\nabla p + \nabla \cdot \left(\rho\nu \left(\nabla \boldsymbol{u} + (\nabla \boldsymbol{u})^{\intercal}\right)\right) + \rho \boldsymbol{g} + \boldsymbol{F}_{\mathrm{L}} + \boldsymbol{F}_{\mathrm{st}} \qquad (1)$$

with $\boldsymbol{u}$, t, ρ, p, ν, $\boldsymbol{g}$, $\boldsymbol{F}_{\mathrm{L}}$ and $\boldsymbol{F}_{\mathrm{st}}$ meaning fluid velocity, time, density, pressure, kinematic viscosity, gravity, Lorentz force and surface tension force. The volume-of-fluid method is used to model the different phases of the battery. The phase

fraction α_i denotes the fraction of fluid i in a single cell – all variable fluid properties (ρ, ν, σ) can be defined by it. The evolution of the phase fraction α_i is calculated by solving the equation

$$\frac{\partial \alpha_i}{\partial t} + \nabla \cdot (\boldsymbol{u}\alpha_i) = 0. \tag{2}$$

The surface tension is computed using the continuum surface force (CSF) model by Brackbill [34]. It is modelled as a volume force around the interfaces as

$$\boldsymbol{F}_{\mathrm{st}} = -\sum_i \sum_{j \neq i} \gamma_{ij} \kappa_{ij} \delta_{ij} \tag{3}$$

with γ_{ij} denoting the interface tension between phases i and j (which is assumed to be constant) and κ_{ij} the curvature of the interface. The force is applied locally around the interface, using some kind of Dirac delta function $\delta_{ij} = \alpha_j \nabla \alpha_i - \alpha_i \nabla \alpha_j$. For a detailed description of the implementation of the volume of fluid method and the surface tension, see [35, 36].

The electric potential ϕ in all fluids is determined by solving the Poisson equation

$$\nabla \cdot (\sigma \nabla \phi) = \nabla \cdot (\sigma \boldsymbol{u} \times \boldsymbol{B}) \tag{4}$$

with σ and $\boldsymbol{B}$ meaning the electric conductivity and magnetic field, respectively. Please note that Neumann boundary conditions force all induced currents to close in the fluid, while Dirichlet boundary conditions allow them to close in the solid current collectors. The electric current $\boldsymbol{J}$ in the battery is then

$$\boldsymbol{J} = -\sigma \nabla \phi + \sigma (\boldsymbol{u} \times \boldsymbol{B}). \tag{5}$$

Using Green's identities we can express the magnetic vector potential $\boldsymbol{A}$ as

$$\boldsymbol{A}(\boldsymbol{r}) = \frac{\mu_0}{4\pi} \int dV \frac{\boldsymbol{J}(\boldsymbol{r}')}{|\boldsymbol{r} - \boldsymbol{r}'|} \tag{6}$$

and thus the magnetic field as $\boldsymbol{B} = \nabla \times \boldsymbol{A} + \boldsymbol{B}_z$. The vertical magnetic background field $\boldsymbol{B}_z$ is a constant. Equations 4, 5 and 6 are solved for each time step in order to compute finally the Lorentz force as $\boldsymbol{F}_{\mathrm{L}} = \boldsymbol{J} \times \boldsymbol{B}$ as source term for the Navier-Stokes equation (equation 1).

3. Instability mechanism We will firstly give a conceptual explanation of the instability mechanism with a simple model of an aluminium reduction cell

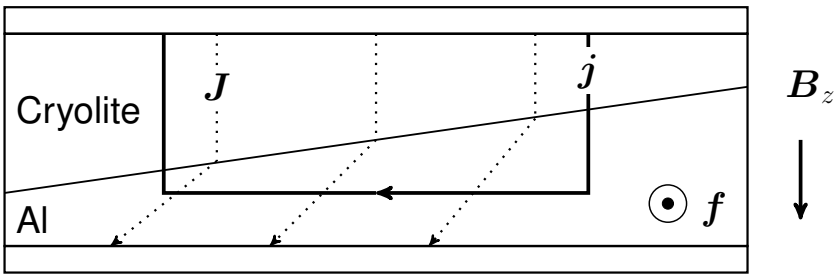

Figure 2: Scheme of an aluminium reduction cell with inclined interface, global current $\boldsymbol{J}$, compensation current $\boldsymbol{j}$, magnetic background field $\boldsymbol{B}_z$ and Lorentz force $\boldsymbol{f}$.

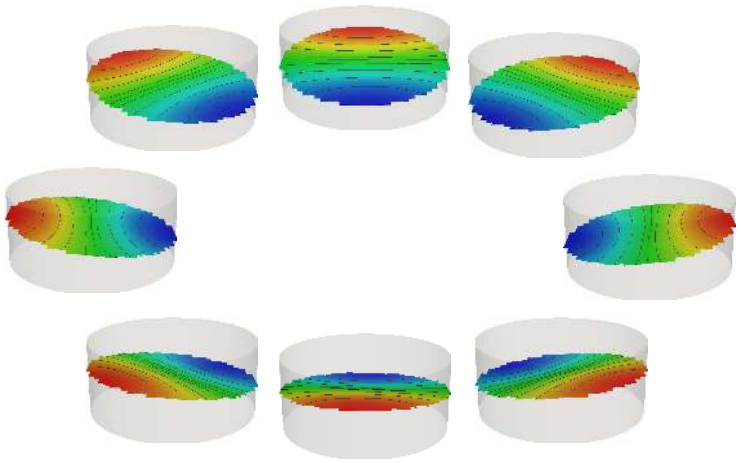

Figure 3: Rotating inclined interface of a two layer system of an aluminium reduction cell.

according to Sele [28]. Such a cell consists of a liquid aluminium layer at the bottom and a cryolite layer at the top (Fig. 2). A vertical electrolysis current is applied by carbon current collectors; the upper electrode is the positive one. The electric conductivity of aluminium is 10^4 times higher than that of cryolite. At certain conditions, a deformation of the Al-cryolite interface starts to rotate (Fig. 3); the initial disturbance may even grow. This instability is known as metal pad rolling, sloshing or long wave instability.

Sele [28] was the first to provide a simple, understandable model for the origin of this movement. For a flat interface, the cell current $\boldsymbol{J}$ is purely vertical. An inclined interface leads to a compensation current $\boldsymbol{j}$ comprising a strong horizontal fraction (Fig. 2). If a vertical magnetic background field $\boldsymbol{B}_z$ is present, the horizontal currents may interact with it, leading to a Lorentz force pointing out of the plane (Fig. 2). If we consider the Lorentz force to displace only the crest of aluminium, it will generate a rotating wave. Note that the disturbed current does not close in the cryolite due to its poor conductivity – it has to close in the upper carbon current collector.

In an LMB, the mechanism is quite similar. We consider a stratification of three phases with inclined interface in 2D. The salt layer is poorly conducting, compared to the metals (Fig. 4a); the chosen values do not belong to a certain LMB, but are of a typical order of magnitude. For computing the electric potential we use Neumann boundary conditions, i.e. the compensation current $\boldsymbol{j}$ has to close in the liquid metals. This is quite realistic for tall electrodes; for flat cells with bad conducting current collectors, a different choice of boundary conditions is probably better suited. Fig. 4b shows the full cell current $\boldsymbol{J}$ – it is concentrated in the well conducting corner. Note that horizontal currents appear only in the metals; in the salt layer the current is almost vertical. Fig. 4c illustrates the perturbed current $\boldsymbol{j}$. Computing the cross product of a vertical magnetic background field and the disturbed current, we obtain the Lorentz force that is aligned with the y-axis (Fig. 4d). It drives the upper metal anti-clockwise and the lower clockwise. The crest turns then anti-clockwise – it is pushed by the Lorentz force in the upper metal.

The Sele model presented above can describe how a rotating flow and also a rotating wave develops. However, it does not explain why the wave amplitude increases in time. This is assumed to be caused by a reflection of the wave crest

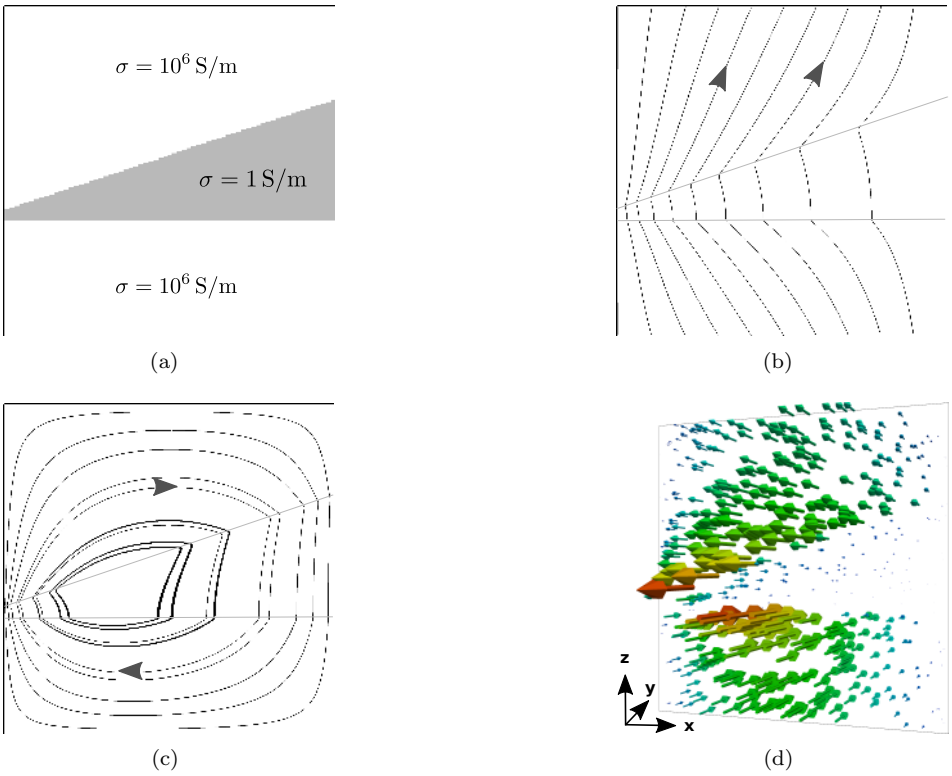

Figure 4: Conductivity (a), complete current (b) and compensation-current (c) as well as Lorentz force of compensation-current and vertical field (d). The prescribed electrical current flows upwards, $\boldsymbol{B}_z$ is pointing upwards.

at the solid walls [37, 31]. Using a wave equation approach [38], Bojarevics and Romerio extended the Sele model by the influence of the cells aspect ratio. Due to the coupling of two waves, cylindrical and quadratic cells are assumed to be always unstable [29] (neglecting several dissipation mechanisms).

4. Metal pad rolling in a 3-layer system First simulations of the 3-phase system of a Mg|NaCl-KCl-$MgCl_2$|Sb battery show metal pad rolling – see Fig. 5a. We use here a simple cell model of height and diameter $h = d = 10\,\mathrm{cm}$, with a 1 cm thick electrolyte layer and 4.5 cm thick electrodes. Denoting the upper metal by 1, the electrolyte by 2 and the lower metal by 3, the densities are [39, 6, 40]

$$\rho_1 = 1577\,\mathrm{kg/m^3} \qquad \rho_2 = 1715\,\mathrm{kg/m^3} \qquad \rho_3 = 6270\,\mathrm{kg/m^3},$$

the viscosities

$$\nu_1 = 6.7 \cdot 10^{-7}\,\mathrm{m^2/s} \qquad \nu_2 = 6.8 \cdot 10^{-7}\,\mathrm{m^2/s} \qquad \nu_3 = 2.0 \cdot 10^{-7}\,\mathrm{m^2/s}$$

and the electric conductivities

$$\sigma_1 = 3.6 \cdot 10^6\,\mathrm{S/m} \qquad \sigma_2 = 80\,\mathrm{S/m} \qquad \sigma_3 = 8.7 \cdot 10^5\,\mathrm{S/m}.$$

The mutual interface tension between the two phases i and j can be estimated using the surface tensions of phase i and j as [41]

$$\gamma_{i|j} = \gamma_i + \gamma_j - 2.0\sqrt{\gamma_i \gamma_j}, \tag{7}$$

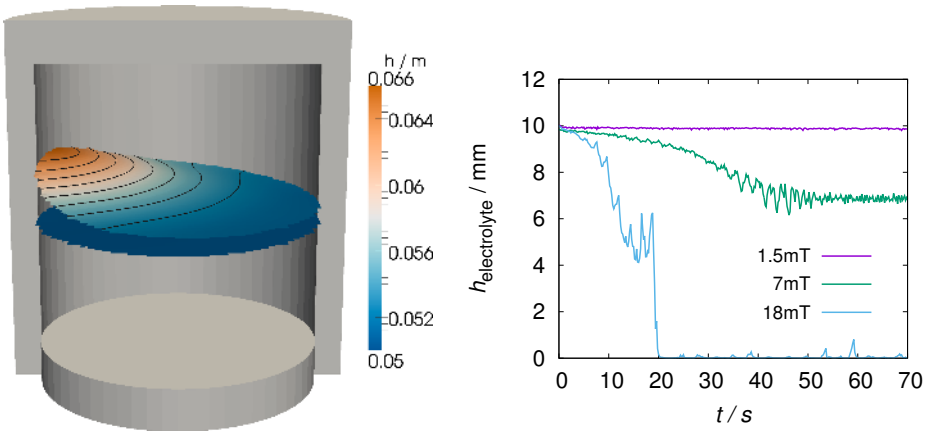

(a) (b)

Figure 5: Illustration of the deformed interface due to metal pad rolling for $B_z = 10\,\mathrm{mT}$ (a) and minimal height of the electrolyte layer for different magnetic background fields and $J = 1\,\mathrm{A/cm^2}$ (b). The minimal distance between the two interfaces shown in (b) rotates; for the rotation period see figure 6.

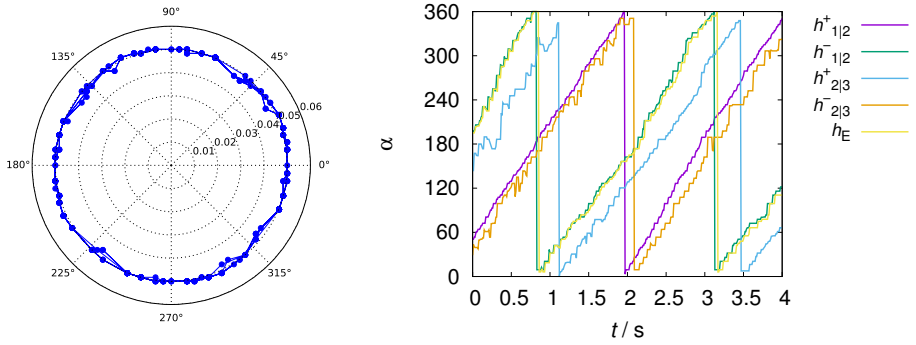

(a) (b)

Figure 6: Radius of minimal electrolyte layer thickness (a) and angle of smallest height h_E as well as minimal h^- and maximal h^+ elevation of both interfaces for a simulation of $I = 200\,\mathrm{A}$ (b).

i.e.

$$\gamma_{1|2} = 0.19\,\mathrm{N/m} \qquad \gamma_{1|3} = 0.016\,\mathrm{N/m} \qquad \gamma_{2|3} = 0.095\,\mathrm{N/m}.$$

We start the simulation with purely horizontal interfaces; the initial disturbance is generated by small numerical errors. We apply a current of 78.5 A which amounts to a current density of about $1\mathrm{A/cm^2}$, that is typical for LMBs. In Fig. 5b we show the minimal electrolyte layer thickness for a vertical magnetic background field between 1.5 and 18 mT. At a field of 7 mT we observe already a deformation of the interface; for values larger than 18 mT a short circuit appears. The values of the magnetic fields are chosen here rather high in order to evidence clearly the effect of metal pad rolling. Realistic vertical fields will probably be smaller than 10 mT.

The crest of electrolyte is well pronounced (Fig. 5a), the trough however,

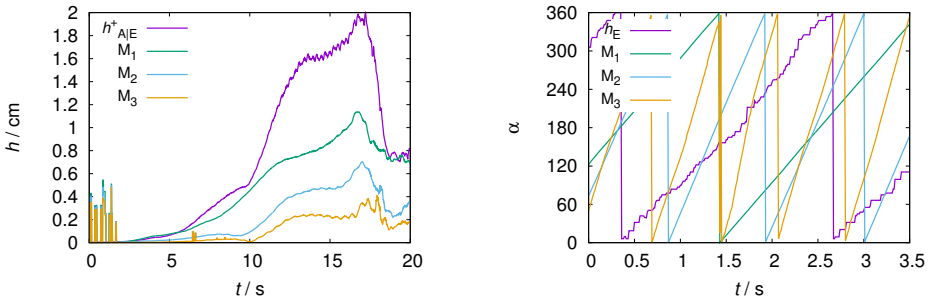

(a) (b)

Figure 7: Amplitude (a) and angle of minimal electrolyte layer thickness and of the azimuthal modes one to three (b) for a simulation of $I = 200\,\mathrm{A}$.

is rather vast and flat. Both rotate with the same speed and with a phaseshift of about 180°. The minimal electrolyte layer thickness is always located at the cylinder wall (Fig. 6a). The same holds for the maximal elevation.

Compared to the upper interface, the lower one deforms only very little. The maximum and minimum elevations all rotate with the same speed, see Fig. 6b. Please note also that the maximum of the lower interface ($h^+_{2|3}$) is always located under the minimum of the upper interface ($h^-_{1|2}$). This promotes the short-circuit.

In order to study the exact shape of the upper interface, we decompose it into several azimuthal modes according to

$$h_{1|2} = \sum_{m=0}^{\infty} (a_m \sin(m\alpha + \beta_m)) \tag{8}$$

with α denoting the angle. At a first glance, the interface deformation in Fig. 5 seems to have only one crest and trough. This corresponds to the mode $m = 1$ with a_m denoting its amplitude and β_m its phase shift. The mode $m = 2$ has then two crests and troughs, and so on. We illustrate now in Fig. 7a the amplitude of the first three modes. As expected, the highest amplitude is observed for $m = 1$; however, the modes $m = 2$ and $m = 3$ still reach about 50 and 25 % of the first one. The higher modes rotate with a shorter period (Fig. 7b): the simulated periods for the first three modes are: $T_1 = 2.18\,\mathrm{s}$, $T_2 = 1.08\,\mathrm{s}$ and $T_3 = 0.76\,\mathrm{s}$ with $I = 200\,\mathrm{A}$ and $B_z = 10\,\mathrm{mT}$.

It is known, that the metal pad roll in aluminium reduction cells oscillates approximately with the frequency of gravity waves. Since the bottom fluid in LMBs is heavy, the 2|3 interface deforms very little. This allows to estimate the frequency of the rotating wave with

$$\omega^2 = \frac{(\rho_2 - \rho_1)gk}{\frac{\rho_1}{\tanh(kh_1)} + \frac{\rho_2}{\tanh(kh_2)}}, \tag{9}$$

that is recognized as the dispersion relation of gravity waves in a 2 layer system [42]. With wavenumber $k = 36.8\,\mathrm{m}^{-1}$ as the first zero of the derivative of the Bessel-function $J_1'(kd/2) = 0$ and $g = 9.81\,\mathrm{m/s}^2$, we find $T_1 = 2.28\,\mathrm{s}$. This confirms that the mode $m = 1$ indeed is a gravity wave. The periods $T_2 \approx T_1/2$ and $T_3 \approx T_1/3$ for $m = 2$ and $m = 3$ are typical for nonlinear harmonics of the fundamental $m = 1$ wave.

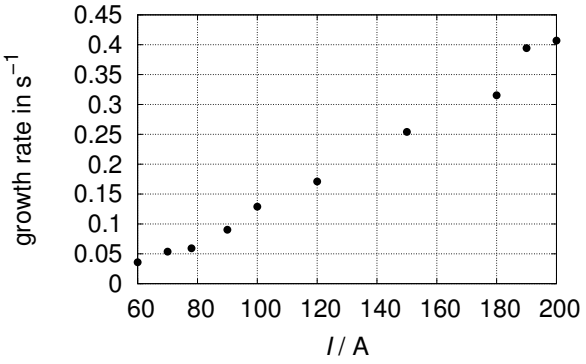

Figure 8: Growth rate of the electrolyte deformation for different electrical currents and $B_z = 10\,\mathrm{mT}$.

In a last step we study the growth rate of the deformation of the interface. Often it is difficult to obtain this growth rate due to the limited electrolyte thickness and possible oscillations of the interface (Fig. 5b). Fig. 8 shows the growth rates for different cell currents. The relation between both appears to be linear; however, the result should be treated with caution, because of the mentioned difficulties in fitting the values.

5. Conclusions and outlook We have developed an integro-differential equation model to simulate metal pad rolling in liquid metal batteries. First simulations are very promising: the expected long wave instability appears (only) at the upper interface of the three-phase system. This is not surprising, since the lower metal remains rather stable due to its high density. As a result, we explained the origin of metal pad rolling in LMBs in close analogy to the known mechanism in aluminium reduction cells. We further described the interface deformation, the growth rate of the instability as well as the period of rotation. Our simulations are another step forward to understand the complex fluid mechanics involved in the operation of large liquid metal batteries.

It is intended to investigate metal pad rolling in liquid metal batteries further. Especially the influence of battery current, magnetic background field and height of the electrolyte layer will be analysed. Comparative studies with the spectral code SFEMaNS [43] are planned for the near future. A validation of our code with experimental findings is in prospect in the long run.

Acknowledgements. This work was supported by Helmholtz-Gemeinschaft Deutscher Forschungszentren in frame of the Helmholtz Alliance “Liquid metal technologies” (LIMTECH). The computations were performed on the HPC-Cluster “Taurus” at the Center for Information Services and High Performance Computing (ZIH) at TU Dresden and on the cluster “Hydra” at Helmholtz-Zentrum Dresden – Rossendorf. We gratefully acknowledge fruitful discussions with Valdis Bojarevics, Andreas Bund, Loïc Cappanera, Julien Commenge, Jochen Fröhlich, Douglas Kelley, Cornel Lalau, Steffen Landgraf, Michael Nimtz, Marco Starace, Jānis Priede and Oleg Zikanov on several aspects of metal pad rolling and liquid metal batteries and Henrik Schulz for the HPC support.

REFERENCES

1. N. Weber, et al. Metal pad roll instability in liquid metal batteries. In *Proceedings of the 10th PAMIR International Conference* (2016).
2. *World Energy Outlook 2013* (International Energy Agency, 2013).
3. R. E. Huggins. *Energy Storage* (Springer, 2016).
4. R. van Noorden. A better battery. *Nature*, vol. 507 (2014), pp. 26–28.
5. D. J. Bradwell. Liquid Metal Batteries: Ambipolar Electrolysis and Alkaline Earth Electroalloying Cells. Ph.D. thesis, Massachusetts Institute of Technology, 2011.
6. H. Kim, et al. Liquid Metal Batteries: Past, Present, and Future. *Chem. Rev.*, vol. 113 (2013), no. 3, pp. 2075–2099.
7. K. B. Hueso, M. Armand, and T. Rojo. High temperature sodium batteries: Status, challenges and future trends. *Energy Environ. Sci.*, vol. 6 (2013), no. 3, p. 734.
8. J. Liu, et al. Materials Science and Materials Chemistry for Large Scale Electrochemical Energy Storage: From Transportation to Electrical Grid. *Adv. Funct. Mater.*, vol. 23 (2013), no. 8, pp. 929–946.
9. E. J. Cairns, et al. *Galvanic Cells with Fused-Salt Electrolytes*. No. ANL-7316 (Argonne National Laboratory, 1967).
10. C. E. Crouthamel and H. L. Recht, editors. *Regenerative EMF Cells*, vol. 64 (American Chemical Society, 1967).
11. E. J. Cairns and H. Shimotake. High-Temperature Batteries. *Science*, vol. 164 (1969), pp. 1347–1355.
12. D. A. J. Swinkels. Molten Salt Batteries and Fuel Cells. In J. Braunstein, G. Mamantov, and G. P. Smith, editors, *Advances in Molten Salt Chemistry*, vol. 1 (Plenum Press, New York, 1971) pp. 165–223.
13. H. L. Chum and R. A. Osteryoung. *Review of Thermally Regenerative Electrochemical Systems* (Solar Energy Research Institute, 1980).
14. H. L. Chum and R. A. Osteryoung. *Review of Thermally Regenerative Electrochemical Cells* (Solar Energy Research Institute, 1981).
15. N. Weber, et al. The influence of current collectors on Tayler instability and electro vortex flows in liquid metal batteries. *Phys. Fluids*, vol. 27 (2015), no. 014103.
16. N. Weber, V. Galindo, F. Stefani, and T. Weier. Current-driven flow instabilities in large-scale liquid metal batteries, and how to tame them. *J. Power Sources*, vol. 265 (2014), pp. 166–173.
17. W. Herreman, C. Nore, L. Cappanera, and J.-L. Guermond. Tayler instability in liquid metal columns and liquid metal batteries. *J. Fluid Mech.*, vol. 771 (2015), pp. 79–114.
18. Y. Shen and O. Zikanov. Thermal convection in a liquid metal battery. *Theor. Comput. Fluid Dyn.*, vol. 30 (2016), no. 4, pp. 275–294.
19. D. H. Kelley and D. R. Sadoway. Mixing in a liquid metal electrode. *Phys. Fluids*, vol. 26 (2014), no. 5, p. 057102.
20. A. Beltrán. MHD natural convection flow in a liquid metal electrode. *Appl. Therm. Eng.*, (2016).
21. H. Kim, D. A. Boysen, T. Ouchi, and D. R. Sadoway. Calcium - bismuth electrodes for large - scale energy storage. *J. Power Sources*, vol. 241 (2013), pp. 239–248.
22. L. A. Herédy, M. L. Iverson, G. D. Ulrich, and H. L. Recht. Development of a thermally regenerative Sodium-Mercury galvanic system Part I Electrochemical and Chemical Behavior of Sodium-Mercury Galvanic Cells. In *Regenerative EMF Cells* (1967) pp. 30–42.

23. B. Agruss and H. R. Karas. The Thermally Regenerative Liquid Metal Concentration Cell. In R. F. Gold, editor, *Regenerative EMF Cells*, vol. 64 of *Advances in Chemistry* (American Chemical Society, Washington, D.C., 1967) pp. 62–81.

24. M. S. Foster. Laboratory Studies of Intermetallic Cells. In *Regenerative EMF Cells* (1967) pp. 136–148.

25. R. C. Vogel, M. Levenson, E. R. Proud, and J. Royal. Chemical engineering division research highlights. Tech. Rep. ANL-7350, Argonne National Laboratory, 1967.

26. T. Ouchi, H. Kim, X. Ning, and D. R. Sadoway. Calcium-Antimony Alloys as Electrodes for Liquid Metal Batteries. *J. Electrochem. Soc.*, vol. 161 (2014), no. 12, pp. A1898–A1904.

27. O. Zikanov. Metal pad instabilities in liquid metal batteries. *Phys. Rev. E*, vol. 92 (2015), no. 063021.

28. T. Sele. Instabilities of the metal surface in electrolytic alumina reduction cells. *Metall. Mater. Trans. B*, vol. 8 (1977), no. 4, pp. 613–618.

29. V. Bojarevics and M. V. Romerio. Long waves instability of liquid metal-electrolyte interface in aluminium electrolysis cell: A generalization of Sele's criterion. *Eur. J. Mech. - BFluids*, vol. 13 (1994), pp. 33–56.

30. P. A. Davidson. *An Introduction to Magnetohydrodynamics*. Cambridge texts in applied mathematics (Cambridge University Press, Cambridge ; New York, 2001).

31. S. Molokov, G. El, and A. Lukyanov. Classification of instability modes in a model of aluminium reduction cells with a uniform magnetic field. *Theor. Comput. Fluid Dyn.*, vol. 25 (2011), no. 5, pp. 261–279.

32. N. Weber, et al. Numerical simulation of the Tayler instability in liquid metals. *New J. Phys.*, vol. 15 (2013), no. 043034.

33. T. Marić, J. Höpken, and K. Mooney. *The OpenFOAM Technology Primer* (Sourceflux, Duisburg, 2014). OCLC: 897180351.

34. J. U. Brackbill, D. B. Kothe, and C. Zemach. A continuum method for modeling surface tension. *J. Comput. Phys.*, vol. 100 (1992), pp. 335–354.

35. O. Ubbink. Numerical prediction of two fluid systems with sharp interfaces. Ph.D. thesis, University of London, 1997.

36. H. Rusche. Computational Fluid Dynamics of Dispersed Two-Phase Flows at High Phase Fractions. Ph.D. thesis, Imperial College London, 2002.

37. A. Lukyanov, G. El, and S. Molokov. Instability of MHD-modified interfacial gravity waves revisited. *Phys. Lett. A*, vol. 290 (2001), pp. 165–172.

38. N. Urata. Magnetics and metal pad instability. *Light Met.*, (1985), pp. 581–591.

39. N. E. Todreas and P. Hejzlar. Flexible Conversion Ratio Fast Reactor Systems Evaluation. Tech. rep., MIT, 2008.

40. C. J. Smithells, W. F. Gale, and T. C. Totemeier. *Smithells Metals Reference Book* (Elsevier Butterworth-Heinemann, Amsterdam ; Boston, 2004), 8th ed.

41. J. N. Israelachvili. *Intermolecular and Surface Forces* (Academic Press, Burlington, MA, 2011), 3rd ed.

42. L. Cappanera. Stabilisation non linéaire des équations de la magnétohydrodynamique et applications aux écoulements multiphasiques. Ph.D. thesis, université Paris-Saclay, 2015.

43. J.-L. Guermond, R. Laguerre, J. Léorat, and C. Nore. Nonlinear magnetohydrodynamics in axisymmetric heterogeneous domains using a Fourier/finite element technique and an interior penalty method. *J. Comput. Phys.*, vol. 228 (2009), no. 8, pp. 2739–2757.